Journal of Solid State Chemistry 210 (2013) 1–9

Contents lists available at ScienceDirect

Journal of Solid State Chemistry

journal homepage: www.elsevier.com/locate/jssc

Cationic disorder and Mn^{3+}/Mn^{4+} charge ordering in the B' and B'' sites of $Ca_3Mn_2NbO_9$ perovskite: a comparison with $Ca_3Mn_2WO_9$

C.A. López [a,b,*], M.E. Saleta [b], J.C. Pedregosa [a], R.D. Sánchez [b], J.A. Alonso [c], M.T. Fernández-Díaz [d]

[a] INTEQUI-Área de Química General e Inorgánica "Dr. G. F. Puelles", Facultad de Química, Bioquímica y Farmacia, Universidad Nacional de San Luis, Chacabuco y Pedernera, 5700 San Luis, Argentina
[b] Centro Atómico Bariloche, Comisión Nacional de Energía Atómica and Instituto Balseiro, Universidad Nacional de Cuyo, 8400S.C. de Bariloche, Río Negro, Argentina
[c] Instituto de Ciencia de Materiales de Madrid, CSIC, Cantoblanco, E-28049 Madrid, Spain
[d] Institut Laue-Langevin, B.P. 156, F-38042 Grenoble Cedex 9, France

ARTICLE INFO

Article history:
Received 1 August 2013
Received in revised form
21 October 2013
Accepted 23 October 2013
Available online 30 October 2013

Keywords:
Double perovskite
Crystal structure
Magnetic behaviour
Transport properties
Charge ordering

ABSTRACT

We describe the preparation, crystal structure determination, magnetic and transport properties of two novel Mn-containing perovskites, with a different electronic configuration for Mn atoms located in *B* site. $Ca_3Mn_2^{3+}WO_9$ and $Ca_3Mn_2^{3+/4+}NbO_9$ were synthesized by standard ceramic procedures; the crystallographic structure was studied from X-ray powder diffraction (XRPD) and neutron powder diffraction (NPD). Both phases exhibit a monoclinic symmetry (S.G.: $P2_1/n$); $Ca_3Mn_2WO_9$ presents a long-range ordering over the *B* sites, whereas $Ca_3Mn_2NbO_9$ is strongly disordered. By "*in-situ*" NPD, the temperature evolution of the structure study presents an interesting evolution in the octahedral size ($\langle$Mn–O$\rangle$) for $Ca_3Mn_2NbO_9$, driven by a charge ordering effect between Mn^{3+} and Mn^{4+} atoms, related to the anomaly observed in the transport measurements at $T \approx 160$ K. Both materials present a magnetic order below $T_C = 30$ K and 40 K for W and Nb materials, respectively. The magneto-transport measurements display non-negligible magnetoresistance properties in the paramagnetic regime.

1. Introduction

Transition metal oxides are currently of significant interest for the development of renewable energy technologies such as solid oxide fuel cells, thermoelectric (TE) modules and high-temperature superconductors [1,2]. Manganites with a perovskite-type structure represent a family of oxides with various remarkable properties, such as ferromagnetism, metallicity and spin/charge ordering phenomena [3].

On the other hand, since the discovery of colossal magnetoresistance (CMR) [4] in manganites there has been an increasing interest of solid-state chemists and physicists in preparing new compounds that could exhibit this property, since this effect is of technological interest for the detection of magnetic fields and in magnetic memory devices. A report about Sr_2FeMoO_6 double perovskite demonstrating that in its electronic structure only minority spins are present at the Fermi level [5], thus exhibiting intrinsic tunnelling-type magnetoresistance (TMR) at room temperature (RT), motivated the study of this material [6,7] and triggered the interest to prepare novel double perovskites which potentially could present half-metallic properties.

Despite the large number of double perovskites informed up to now, few studies are devoted to compounds with $A_3B'_2B''O_9$ stoichiometry. This particular type of stoichiometry is apparently more complex, but these oxides are also double perovskites $A_2B'_{1.33}B''_{0.66}O_6$ whose crystallographic formula can be re-written as $A_2[B']_a[B'_{1/3}B''_{2/3}]_bO_6$, where *a* and *b* denote the crystallographic sites in the corresponding space group. Thus, they display an intrinsic partial disordering over half of the perovskite ($B'_{1/3}B''_{2/3}$) positions. Furthermore, this composition offers the possibility of changing the oxidation states of the B' and B'' ions and consequently modifying the electrical and magnetic properties. Some double perovskites have been reported as ferrimagnets with T_C's, in some cases, above RT. Previously we have prepared and studied the magnetic properties of some double perovskites with B'=Fe, as $Sr_3Fe_2MoO_9$, $Ca_3Fe_2WO_9$, $Sr_3Fe_2UO_9$ and $Sr_3Fe_2TeO_9$ and observed a ferrimagnetic behaviour below $T_C = 280$ K, 310 K, 330 K and 717 K respectively [8–11]. Also, we have induced a semi-metallic behaviour and CMR properties in these compounds, as that recently reported in $Sr_3Fe_2MoO_9$ via chemical reduction, by topotactical removal of oxygen atoms [12].

* Corresponding author at: INTEQUI-Área de Química General e Inorgánica "Dr. G. F. Puelles", Facultad de Química, Bioquímica y Farmacia, Universidad Nacional de San Luis, Chacabuco y Pedernera, 5700 San Luis, Argentina.
Tel.: +54 266 442 3370.
E-mail addresses: calopez@unsl.edu.ar, calclopez@gmail.com (C.A. López).

0022-4596/$ - see front matter Crown Copyright © 2013 Published by Elsevier Inc. All rights reserved.
http://dx.doi.org/10.1016/j.jssc.2013.10.039

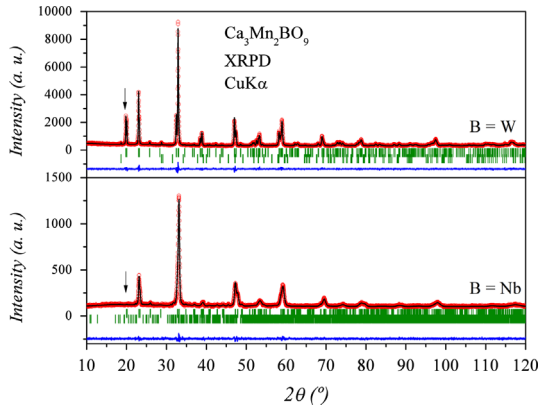

Fig. 1. Room temperature X-ray powder diffraction data (circles) and Rietveld simulated line profiles (full line) for $Ca_3Mn_2WO_9$ and $Ca_3Mn_2NbO_9$ double perovskites. The line at the bottom is the difference between calculated and experimental patterns for each sample. The upper set of bars corresponds to the Bragg reflections for the main phase and the lower set of bars corresponds to the Bragg reflections for the $CaWO_4$ and $Ca_4Nb_2O_9$ impurity phase in CMW and CMN respectively. The arrows indicate the positions of the superstructure diffractions (0 1 1) in both patterns.

A main finding is that these intrinsically "disordered" double perovskites, containing a random distribution of Fe and Mo, W, U or Te at the B'' positions, exhibit a strong magnetic scattering on the low-angle Bragg positions of the neutron diffraction patterns, originating upon naturally-occurring islands of Fe^{3+} cations in which strong antiferromagnetic (AFM) Fe–O–Fe super-exchange interactions are promoted, similar to those existing in the $LaFeO_3$ perovskite.

With the same stoichiometries, phases with B'=Cr (such as $A_3Cr_2B''O_9$ for A=Ca, Sr and Ba and B''=W and Mo) [13,14]; B'=In (as $Sr_3In_2B''O_9$ for B''=W and U) [15] and B'=Co (as $La_3Co_2B''O_9$ for B''=Nb, Ta and Sb) [16,17], have also been reported. There are no previous reports with manganese at site B'; this transition element is specially interesting since it can be present in different oxidation states (Mn^{2+}, Mn^{3+} or Mn^{4+}) depending on the partner ions in the perovskite. The mixed oxidation state is responsible for different properties observed in Mn materials with perovskite structure, such as a ferromagnetism, metal-like conductivity and magnetoresistance. Also, the mixed oxidation state can drive charge ordering and orbital ordering effects. Both are well known in simple perovskites. Charge and orbital ordering in half-doped simple perovskites, which are also accompanied by antiferromagnetic (AFM) spin ordering, form a fascinating class of physical phenomena. The half-doped manganites, in which these phenomena have been most investigated, belong to the system with general formula $A_{0.5}Ca_{0.5}MnO_3$, with A site being occupied by trivalent elements like La, Pr, Nd, Sm, Y, etc. However, the charge ordering and orbital ordering effects are rare in double-perovskite oxides. In these structures, the ratio between the different Mn oxidation states can be tuned by using adequate cations with suitable oxidation states at the B'' site, such as W^{6+} and Nb^{5+}. In this work we have designed, prepared and characterized $Ca_3Mn_2NbO_9$ and $Ca_3Mn_2WO_9$ double perovskites, which exhibit a very distinct phenomenology. They have been investigated by x-ray powder diffraction (XRPD) and neutron powder diffraction (NPD), in complement with magnetization and magneto-transport measurements.

2. Experimental

$Ca_3Mn_2B''O_9$ double perovskites with B''=W and Nb were prepared as black polycrystalline powders by solid-state reactions. Stoichiometric amounts of analytical grade $CaCO_3$, $MnCO_3$ and WO_3 (or Nb_2O_5) were mixed, ground, placed in a platinum crucible and treated at 800 °C in air for 12 h. In the following treatments, the resulting powder was reground and the temperature of the thermal treatment was increased by 100 °C in each step until a pure compound was obtained. The rate of heating was of 5 °C/min. Final temperatures of 1400 and 1100 °C were required to obtain $Ca_3Mn_2WO_9$ (labelled CMW) and $Ca_3Mn_2NbO_9$ (labelled CMN) respectively.

The reaction progress and the initial identification and characterization of the samples were carried out by XRPD. The experimental XRPD patterns obtained on a diffractometer Rigaku D-MAX-IIIC with Cu$K\alpha$ (λ=1.5418 Å) radiation; the 2θ range was 10° up to 120° with increments of 0.02° and the counting time was 4 s/step. In order to study the crystallographic structures at room temperature (RT), NPD patterns were collected on the HRPT diffractometer (Paul Scherrer Institute, Villigen, Switzerland) with a wavelength of 1.494 Å. The sequential study of the crystallographic and magnetic structures at low temperature was carried out by NPD patterns collected on the D20 diffractometer (ILL, Grenoble, France) with a wavelength of 2.492 Å. Both XRPD and NPD diffraction patterns were analysed with the Rietveld method using the FullProf programme [18,19].

The Mn oxidation state was determined by thermogravimetric analysis performed in a Shimadzu TG-50H thermal analyser apparatus using flowing H_2/N_2(5%/95%) at 50 mL/min from 25 °C to 1000 °C, at a heating rate of 5 °C/min. About 18 mg of the sample was used in the experiment.

The magnetic measurements were performed in a commercial superconducting quantum interference device (SQUID-Quantum Design MPMS-5S) magnetometer in the $5 \le T \le 300$ K temperature range with an external magnetic field H=10 kOe. Transport and magnetotransport measurements were performed by the conventional four probe technique, under magnetic fields up to 90 kOe in a PPMS system from Quantum Design. For the resistance and magnetotransport measurements, powders of CMW and CMN were pressed in bar-shaped pellets and sintered at the same final temperature used in the synthesis.

3. Results

$Ca_3Mn_2WO_9$ and $Ca_3Mn_2NbO_9$ were obtained as a well-crystallized polycrystalline powders. Fig. 1 shows the XRPD patterns; the structures are refined in a monoclinic $P2_1/n$ model, as described in Section 3.2.1.

3.1. Thermogravimetric analysis (TGA)

Fig. 2 shows the thermal evolution of weight loss obtained by TGA (in H_2/N_2 5%/95%) methods of the CMW and CMN samples. The final products of the reduction process were identified by XRPD allowing us to propose the following reactions:

CMW: $Ca_3Mn_2WO_9 + H_2 \rightarrow Ca_2MnWO_6 + MnO + CaO + H_2O$

CMN: $Ca_3Mn_2NbO_9 + 2H_2 \rightarrow CaNbO_3 + 2\ nO + 2CaO + 2H_2O$

The theoretical weight loss for these reactions was 2.87% and 6.85% for CMW and CMN respectively. These values are in agreement with the experimental ones (2.9% and 6.5%). These facts indicate that all Mn ions are only in the Mn^{3+} state in CMW. However, Mn ions present an average oxidations state of +3.5 in CMN (Mn^{3+}/Mn^{4+}=1).

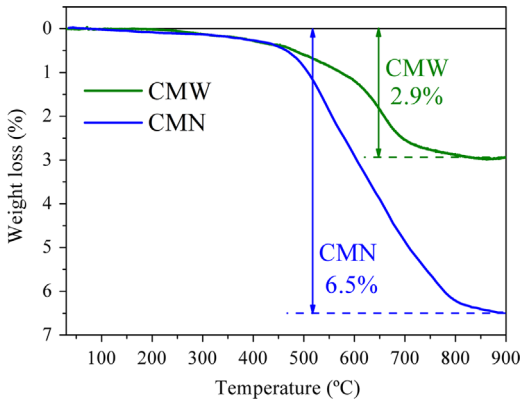

Fig. 2. TGA curves of CMW and CMN samples obtained in H_2/N_2 (5%/95%) flow at 50 mL/min, at heating rate of 5 °C/min.

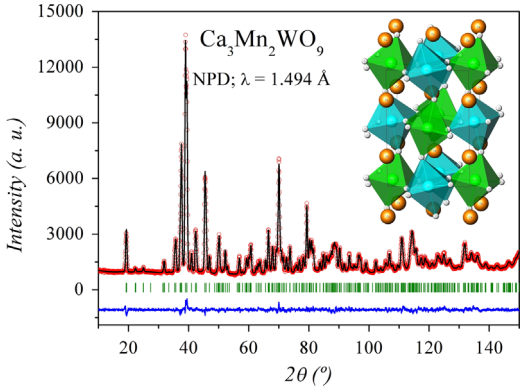

Fig. 3. Rietveld plots after the refinement of the crystal structure of $Ca_3Mn_2WO_9$ from NPD data at 295 K. The line at the bottom is the difference between calculated and experimental patterns. The set of bars corresponds to the Bragg reflections. The inset is a view of the monoclinic crystal structure of CMW double perovskite; each $[Mn]_{2d}O_6$ octahedron (cyan colour) is corner linked to six $[Mn_{0.33}W_{0.66}]_{2c}O_6$ octahedra (green colour). The white and orange spheres correspond to oxygen and calcium atoms respectively. (For interpretation of the references to colour in this figure legend, the reader is referred to the web version of this article.)

3.2. Structure at room temperature

3.2.1. Structural refinement by XRPD

Both compounds were initially indexed with a monoclinic unit cell and the structure was refined as monoclinic in the space group (SG) $P2_1/n$ (no. 14). For this monoclinic symmetry the tilting system is $a^+b^-b^-$, and the unit-cell parameters are related to a_0 (ideal cubic perovskite, $a_0 \approx 3.9$ Å) as $a \approx b \approx \sqrt{2}a_0$ and $c \approx 2a_0$. Ca atoms were located at the 4*e* (*x*,*y*,*z*) positions, Mn/*B*″ at 2*c* (1/2,0,1/2) and at 2*d* (1/2,0,0) sites, and oxygen atoms at 4*e*. For this space group $P2_1/n$ (derived to ideal cubic double perovskite $Fm\bar{3}m$) there are two possible sites for *B* type cations, namely, 2*c* and 2*d*. Minor amounts of $CaWO_4$ (SG: *I*4/*a*) [20], and $Ca_4Nb_2O_9$ (S.G.: $P2_1/c$) [21], were included in the refinement as secondary phases for CMW and CMN respectively. From the scale factors of the main and secondary phases, the following amounts of impurities were determined as 0.5% of $CaWO_4$ and 1% of $Ca_4Nb_2O_9$ in CMW and CMN respectively. The good agreement between the observed and calculated XRPD patterns after the refinement is shown in Fig. 1.

In double perovskites with stoichiometry $A_2B'B''O_6$ the *B*′ and *B*″ cations can be totally ordered, which corresponds to a crystallographic formula $A_2[B']_{2c}[B'']_{2d}O_6$ for this monoclinic symmetry. For perovskites with stoichiometry $A_3B'_2B''O_9$, total order is intrinsically impossible. Thus, if one wants to assure certain degree of disorder in this kind of perovskites, the $A_3B'_2B''O_9$ stoichiometry is ideal. In order to obtain a better picture of the distribution of the *B* cations in the two crystallographic sites and to consider the degree of disorder, we can write the crystallographic formula as $A_2[B'_{1-\alpha}B''_{\alpha}]_{2c}[B'_{(1/3)+\alpha}B''_{(2/3)-\alpha}]_{2d}O_6$, where $0 \le \alpha \le 1/3$. Thus, if $\alpha=0$ we have maximum order (but not full order), and if $\alpha=1/3$ we have maximum disorder. The composition for maximum disorder, i.e. $A_2[B'_{2/3}B''_{1/3}]_{2c}[B'_{2/3}B''_{1/3}]_{2d}O_6$, corresponds to *B* cations randomly distributed. Based on the preceding discussion we can define the degree of order (DO) as DO=1–3α. For maximum order DO=1 (within the intrinsic disorder) and for random distribution DO=0. DO values are obtained from the refinements of occupancies of *B* cations in 2*c* and 2*d* sites.

The CMW pattern shows well-defined superstructure reflections (0 1 1) and (0 1 3) arising from the Mn/W ordering over both *B* positions due to the charge difference between Mn^{3+} and W^{6+} cations. Contrarily, the CMN pattern shows no superstructure reflections (Fig. 1). The smaller charge difference between Mn^{3+}–Mn^{4+} and Nb^{5+}, accounts for the disorder over the two sites, thus reducing the difference in scattering power and hence the intensity of the superstructure reflections. Therefore, from XRPD the sample CMW is completely ordered but CMN is disordered.

The full disorder in CMN implies that Mn and Nb ions are in the same crystallographic sites, as a simple perovskite Ca $[Mn_{0.66}Nb_{0.33}]O_3$. For this reason we also checked the *Pnma* space group that presents the same tilting system ($a^+b^-b^-$) that $P2_1/n$ space group and is used to describe the simple perovskite (ABO_3) for a single *B* atom. For this orthorhombic symmetry the unit cell parameters are related to a_0 as $a \approx c \approx \sqrt{2}a_0$ and $b \approx 2a_0$. Ca atoms were located at the 4*c* (*x*,1/4,*z*) site, Mn/*B*″ at 4*b* (1/2,0,0) site, and oxygen atoms at 4*c* (*x*,1/4,*z*) and 8*d* (*x*,*y*,*z*) sites. The diffraction pattern also can be fitted in the *Pnma* space group, getting a similar agreement factor to the $P2_1/n$ model.

The difference between $P2_1/n$ (fully disordered) and *Pnma* model is very subtle and is mainly due to the oxygen positions. For the $P2_1/n$ model the oxygen atoms are located in three different positions, however, for the *Pnma* model the oxygen atoms are located in only two independent sites. This issue required a further analysis by NPD, neutrons being very sensitive to the oxygen positions.

3.2.2. Structural refinement by NPD

The structural refinements at room temperature from high resolution NPD data for CMW were performed in the $P2_1/n$ space group, as indicated for the XRPD refinement. Fig. 3 illustrates the quality of the agreement between the observed and calculated NPD profiles at RT; the inset shows the schematic view of crystal structure for CMW. The structural parameters at room temperature are listed in Table 1. Brown's phenomenological Bond-Valence Model (BVS) [22] can also help to give an estimation of the actual valence of Mn cations by means of an empirical relationship between the observed bond lengths (Table 1) and the valence of a bond. This calculation can only be applied to the 2*d* site that does not contain a mixed Mn/W occupancy. The valence is the sum of the individual bond valences (s_i), which are calculated as $s_i=\exp[(r_0-r_i)/0.37]$, where r_0 for the Mn^{3+}–O^{2-} pair is 1.76 Å. The bond valences of Mn at 2*d* sites are +3.08(1) in good agreement with the oxidations state calculated by TGA experiments.

The NPD data for CMN were fit with the $P2_1/n$ and *Pnma* space groups, as double and simple perovskites, respectively. Both refinements show an excellent agreement between the observed and calculated patterns, and their agreement factor was acceptable. In order to analyse both models more deeply, we examined the nuclear density in the crystallographic planes where the oxygen atoms with wrong interatomic distances are situated (planes (0 0 2) for $P2_1/n$ and (0 2 0) for *Pnma*). This analysis was

carried out from difference Fourier maps (DFM) obtained from the GFourier programme, [23]. These maps show the difference between the observed and calculated nuclear density (for NPD data). Fig. 4 show the DFMs in equivalent planes for (a) $P2_1/n$ (0 0 2) and (b) *Pnma* (0 2 0). In the colour scale (right side of Fig. 4) the red colour shows positive nuclear density in the observed pattern, absent in the calculated pattern (missing atoms); blue colour indicates negative nuclear density in calculated pattern non-existent in the observed pattern (atoms incorrectly placed). The comparison of the two maps is enlightening: for the $P2_1/n$ space group the missing nuclear density is insignificant, whereas the map corresponding to *Pnma* shows the presence of misplaced atoms; we conclude that $P2_1/n$ is the correct structural model for the crystal structure of CMN.

For CMN, some minor impurity phases were identified and included in the refinement: $Ca_4Nb_2O_9$ (SG: $P2_1/c$) (also observed in XRPD) [21], $CaMnO_3$ (SG: *Pnma*) [24] and $CaNb_2O_6$ (SG: *Pbcn*) [25]. From the scale factors of the main and secondary phases less than 1% in weight was found for the different impurities. Fig. 5 illustrates the quality of the agreement between the observed and calculated NPD profile at RT and the inset shows the schematic view of crystal structure for CMN. The structural parameters at room temperature are listed in Table 2.

The monoclinic crystal structures of both phases (inset in Figs. 3 and 5) contain alternating octahedra (MnO_6 and (Mn,W)O_6 for CMW and (Mn,Nb)O_6 and (Mn,Nb)O_6 for CMN), tilted in phase along the (1 0 0) direction of the pseudo-cubic cell and in anti-phase along the (0 1 0) and (0 0 1) directions, which corresponds to the $a^+b^-b^-$ Glazer's notation as derived by Woodward [26], for 1:1 ordering double perovskites, consistent with the space group $P2_1/n$. The average tilting angles can be estimated as $\varphi=(180-\theta)/2$ where $\theta=\langle B'_{2c}\text{–O–}B''_{2d}\rangle$; we obtain $\varphi=13.4^\circ$ and 13.3° for CMW and CMN respectively.

Table 1
Crystallographic data for CMW phase from NPD data at 295 K. System: Monoclinic, Space group: $P2_1/n$, $Z=2$. Unit-cell parameters: $a=5.41726(8)$ Å, $b=5.51132(9)$ Å, $c=7.6681(1)$ Å, $\beta=90.033(3)^\circ$ and $V=228.941(6)$ Å^3.

Atom	Wyckoff site	x/a	y/b	z/c	B_{iso} (Å^2)	Occ.
(a) Positions, thermal and occupancy factors						
Ca^{2+}	4*e*	0.9930(5)	0.0435(3)	0.2532(7)	1.19(3)	1
Mn^{3+}	2*d*	0.5	0	0	0.69(6)	1
Mn^{3+}	2*c*	0.5	0	0.5	0.8(1)	0.33
W^{6+}	2*c*	0.5	0	0.5	0.8(1)	0.67
$O^{2-}1$	4*e*	0.0791(3)	0.4780(2)	0.2462(4)	0.97(3)	1
$O^{2-}2$	4*e*	0.7070(6)	0.2991(5)	0.0382(5)	0.98(7)	1
$O^{2-}3$	4*e*	0.2044(6)	0.2119(5)	0.9571(5)	1.16(7)	1
$R_p=2.90\%$; $R_{wp}=3.67\%$; $R_{exp}=2.45\%$; $\chi^2=1.16$; $R_{Bragg}=3.06\%$						
$[Mn]_{2d}O_6$ octahedral	(Å)	AO_{12} polyhedral	(Å)			
(b) Main distances and angles Mn–O1 (× 2)	1.997(3)	Ca–O1	3.146(2)			
Mn–O2 (× 2)	2.015(3)	Ca–O1	2.446(2)			
Mn–O3 (× 2)	2.009(3)	Ca–O1	3.120(3)			
⟨Mn–O⟩	2.007(3)	Ca–O1	2.345(3)			
$[Mn/W]_{2c}O_6$ octahedral	(Å)	Ca–O2	2.667(5)			
(Mn/W)–O1(× 2)	1.939(3)	Ca–O2	2.352(5)			
(Mn/W)–O2(× 2)	1.957(3)	Ca–O2	3.344(5)			
(Mn/W)–O3(× 2)	1.964(3)	Ca–O2	2.623(6)			
⟨(Mn/W)–O⟩	1.954(3)	Ca–O3	2.710(6)			
Mn–O1–(Mn/W) (× 2)	153.8(4)°	Ca–O3	3.307(5)			
Mn–O2–(Mn/W) (× 2)	153.1(3)°	Ca–O3	2.389(5)			
Mn–O3–(Mn/W) (× 2)	153.1(3)°	Ca–O3	2.593(5)			
⟨Mn–O–(Mn/W)⟩	153.3°	⟨Ca–O⟩	2.754			

3.3. Magnetic susceptibility

The magnetization vs. temperature data of CMW and CMN samples are displayed in Fig. 6. Both samples present a paramagnetic like magnetization behaviour above ~40 K, while at low temperatures the CMW sample present a maximum at 25 K and CMN sample saturates below 15 K. In all the temperature range, the magnetization values of CMW are higher than those measured for CMN. The inverse of the magnetic susceptibility shows a small shoulder for CMN around ≈ 120 K. A Curie–Weiss fit above 150 K gives paramagnetic moments of 4.98 and 4.40μ_B/Mn for CMW and CMN, respectively, whereas the corresponding Weiss temperatures are +1.4 K and −99 K. The negative θ_{Weiss} indicates clearly the predominance of antiferromagnetic interactions. For CMW the paramagnetic moment is in excellent agreement with that calculated for high-spin Mn^{3+} ($3d^4$, $S=2$, $\mu_{eff}=4.90\mu_B$), as corresponding to the formula $Ca_3Mn_2^{3+}WO_9$. Also, for CMN the paramagnetic moment is close to that expected for an admixture of Mn^{3+} and Mn^{4+} ($\mu_{eff}=4.42\mu_B$), which can be represented by $Ca_3Mn_2^{3+/4+}NbO_9$. From the derivative of the magnetization (see inset of Fig. 6) the temperature of both magnetic transitions can be clearly observed. The T_C's are 30 and 40 K for CMW and CMN, respectively. However, an additional anomaly is observed for CMN at 120 K. The slope of the χ^{-1} vs. T plot is unchanged above and below this temperature (120 K). This means that the Curie constant and hence the effective magnetic moment is constant in the paramagnetic region. However, the θ_{Weiss} value shifts when the data below or above 120 K are considered: this is an indication that the strength of the magnetic interactions is changed in $Ca_3Mn_2^{3+/4+}NbO_9$.

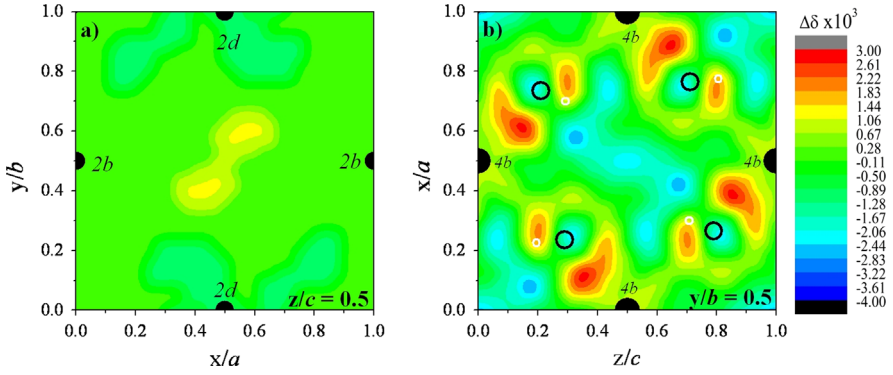

Fig. 4. Difference Fourier Maps for CMN sample where the colour scale represents the nuclear density obtained from a neutron pattern refinement: (a) $P2_1/n$ space group, showing the (0 0 2) plane and (b) *Pnma* space group, showing the (0 2 0) plane. The black filled circles correspond to *B* sites and the open circles correspond to oxygen atoms according to *Pnma* space group. The white circles indicate the oxygen positions obtained with a $P2_1/n$ model. (For interpretation of the references to colour in this figure, the reader is referred to the web version of this article.)

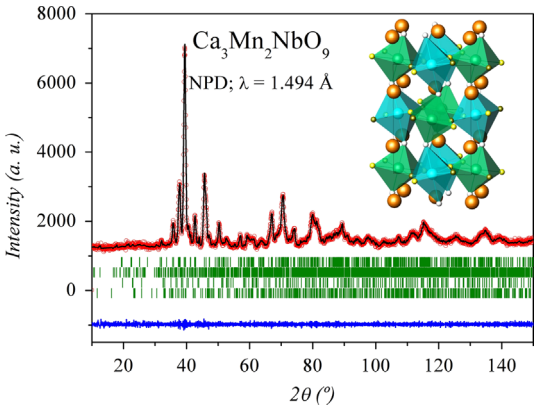

Fig. 5. Rietveld plots after the refinement of the crystal structure of $Ca_3Mn_2NbO_9$ from NPD data at 295 K. The line at the bottom is the difference between calculated and experimental patterns. The upper set of bars corresponds to the Bragg reflections for the main phase and the follow set of bars corresponds to the Bragg reflections for the $Ca_4Nb_2O_9$, $CaMnO_3$ and $CaNb_2O_6$ impurity phases. The inset is a view of the monoclinic crystal structure of CMN double perovskite.

Table 2
Crystallographic data for CMN phase from NPD data at 295 K. System: Monoclinic, space group: $P2_1/n$, $Z=2$. Unit-cell parameters: $a=5.4021(3)$ Å, $b=5.4766(2)$ Å, $c=7.6074(3)$ Å, $\beta=90.253(5)^\circ$ and $V=225.06(2)$ Å^3.

Atom	Wyckoff site	x/a	y/b	z/c	B_{iso} (Å^2)	Occ.
(a) Positions, thermal and occupancy factors						
Ca^{2+}	4*e*	0.986(2)	0.043(2)	0.247(3)	1.9(2)	1
$Mn^{3+/4+}$	2*d*	0.5	0	0	0.8[a]	0.654(8)
Nb^{5+}	2*d*	0.5	0	0	0.8[a]	0.346(8)
$Mn^{3+/4+}$	2*c*	0.5	0	0.5	0.8[a]	0.679(8)
Nb^{5+}	2*c*	0.5	0	0.5	0.8[a]	0.321(8)
$O^{2-}1$	4*e*	0.081(1)	0.483(1)	0.229(1)	0.3(1)	1
$O^{2-}2$	4*e*	0.695(2)	0.275(2)	0.042(1)	1.8(2)	1
$O^{2-}3$	4*e*	0.208(2)	0.200(2)	0.962(1)	1.4(2)	1
$R_p=1.92$; $R_{wp}=2.42\%$; $R_{exp}=2.55\%$; $\chi^2=0.92$; $R_{Bragg}=2.5\%$						
$[Mn/Nb]_{2d}O_6$ octahedral	(Å)		AO_{12} polyhedral		(Å)	
(b) Main distances and angles						
(Mn/Nb)–O1 (× 2)	2.110(6)		Ca–O1		3.11(1)	
(Mn/Nb)–O2 (× 2)	1.864(9)		Ca–O1		2.47(1)	
(Mn/Nb)–O3 (× 2)	1.943(8)		Ca–O1		3.09(1)	
⟨(Mn/Nb)–O⟩	1.972(3)		Ca–O1		2.37(1)	
$[Mn/Nb]_{2c}O_6$ octahedral	(Å)		Ca–O2		2.55(2)	
(Mn/Nb)–O1 (× 2)	1.799(6)		Ca–O2		2.39(2)	
(Mn/Nb)–O2 (× 2)	2.084(9)		Ca–O2		3.30(2)	
(Mn/Nb)–O3 (× 2)	2.011(9)		Ca–O2		2.70(2)	
⟨(Mn/Nb)–O⟩	1.965(3)		Ca–O3		2.63(2)	
$[B]_{2b}$–O1–$[B]_{2d}$(× 2)	153.2(3)°		Ca–O3		3.34(2)	
$[B]_{2b}$–O2–$[B]_{2d}$(× 2)	153.9(4)°		Ca–O3		2.32(2)	
$[B]_{2b}$–O3–$[B]_{2d}$(× 2)	153.2(7)°		Ca–O3		2.63(2)	
⟨$[B]_{2b}$–O–$[B]_{2d}$⟩	153.4°		⟨Ca–O⟩		2740	

[a] Fixed parameters.

In Fig. 7, we plot Zero Field Cooled (ZFC) and Field Cooled (FC) magnetization curves for CMW and CMN measured at low (100 Oe) and at high (5 kOe) magnetic field. These values are compared with a magnetization curve measured at 10 kOe. At low temperatures, a shift between ZFC and FC magnetization curves ($M(ZFC) < M(FC)$) is observed in both samples, even when a high magnetic field is applied (see Fig. 7). This difference between ZFC and FC curves indicates the presence of different magnetic ground states reached at low temperature. The multiple ground states are consequence of the microscopic competition between ferromagnetic and antiferromagnetic interactions present in the system. The magnetic moment frustrated configuration reached at low temperature depends of the magnetic and thermal history.

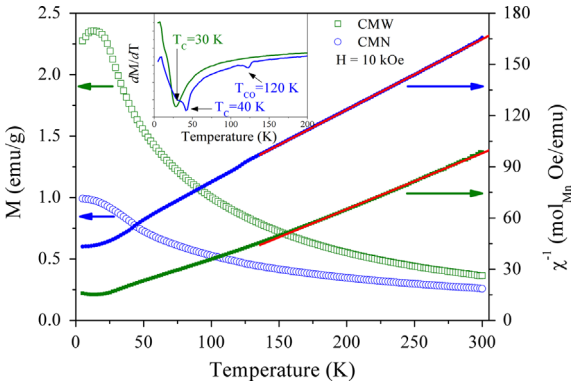

Fig. 6. Magnetization (left axis) and reciprocal susceptibility (right axis) as a function of temperature for CMW and CMN at 10 kOe; the solid lines (red on line) correspond to the Curie–Weiss fits at high temperature. The inset figure shows the first derivate of the magnetization vs. temperature curve, the minima show the transition temperatures. (For interpretation of the references to colour in this figure legend, the reader is referred to the web version of this article.)

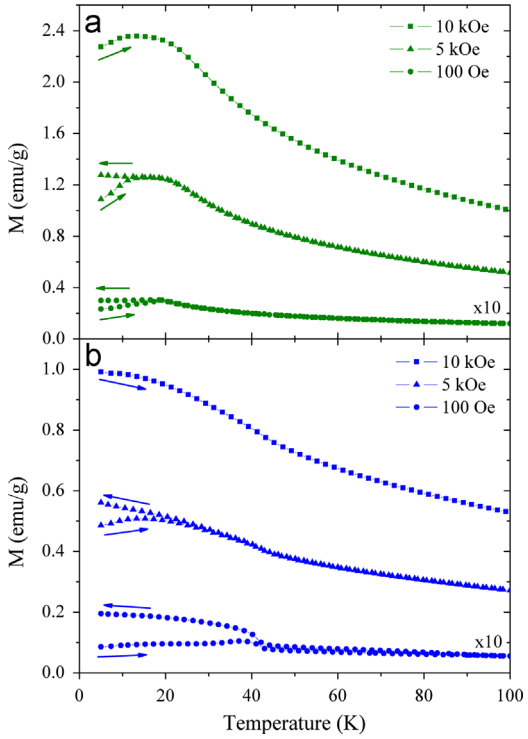

Fig. 7. ZFC and FCC magnetizations at 5 and 0.1 kOe in comparison whit a ZFC measurements at 10 kOe for (a) CMW and (b) CMN.

3.4. Transport and magnetotransport properties

The electrical resistivity (ρ) as a function of temperature is shown in Fig. 8(a) for CMW and CMN samples. The experimental data were obtained from room temperature down to 110 K and 100 K for CMW and CMN, respectively; below this temperature the resistance was out of range in our experimental set-up. At RT the values of resistivity are 33 and 9 Ω cm for CMW and CMN respectively. In both cases the resistivity increases diminishing the temperature, showing a semiconducting-like or thermally activated behaviour. In the inset of Fig. 8(a) a plot of $\ln(\rho)$ vs. T^{-1} clearly shows a linear behaviour. This can be associated with a thermally-activated electronic conduction mechanism ($\rho=\rho_0 \exp(E_g/kT)$). From the linear fit, the obtained activation energies (E_g) are 0.16 and 0.15 eV for CMW and CMN, respectively. These E_g values would correspond to the energy gaps between the valence

and the conduction bands, very similar for both compounds. However, as shown in Fig. 8(a), an additional change is also observed for CMN at 160 K. In the ρ vs. T plot a subtle increase in the resistivity around 160 K is observed. This anomaly is more clearly seen in the $d\ln(\rho)/d(kT)^{-1}$ vs. T plot (lower panel of Fig. 8).

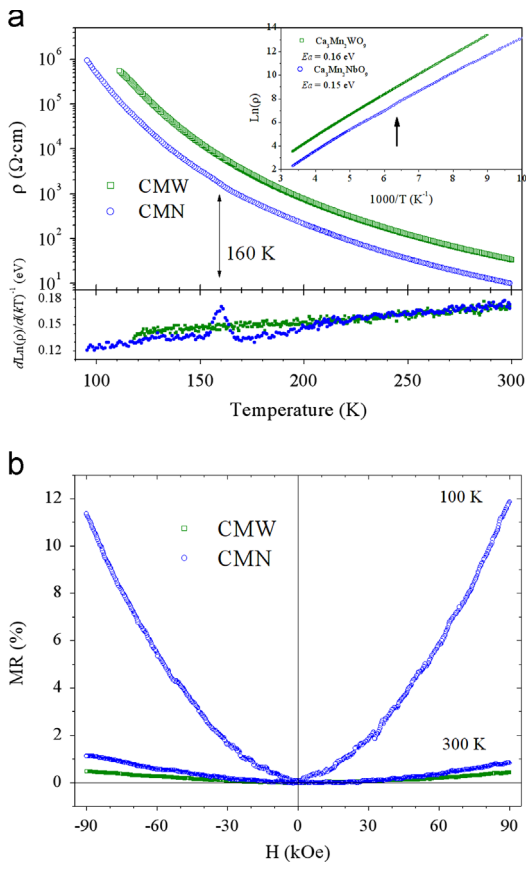

Fig. 8. (a) Electrical resistivity as a function of temperature for CMW and CMN, and inset shows the linear behaviour in Ln(ρ) vs. T^{-1} plot. Bottom: $d\mathrm{Ln}(\rho)/d(kT)^{-1}$ vs. T plot. (b) Magnetoresistance as a function of magnetic field for CMW at 300 K and CMN at 300 K and 100 K.

The electrical resistance was also measured under an external magnetic field at 300 and 100 K (up to $H=9$ T). From this measurement the thermal evolution of the magnetoresistance, was calculated as $\mathrm{MR}(H)=100\times[\rho_{(H)}-\rho_0/\rho_0]$, where ρ_0 is the resistivity at $H=0$ T. A positive magnetoresistance is observed, as shown in Fig. 8(b), reaching a maximum value of 0.5% and 1.2% for CMW and CMN respectively at 300 K. For CMN it was also possible to measure the MR(H) at 100 K, reaching around 11.5% of positive magnetoresistance at 9 T.

3.5. Structure at low temperature

In order to explore with more detail the structural correlations with the observed magnetic and transport properties, we have collected NPD data at low temperatures. From these data we have analysed the crystallographic and magnetic structures.

3.5.1. Crystallographic structure

The thermal evolution of the crystal structures was analysed from a set of NPD ($\lambda=2.492$ Å) patterns sequentially collected in the temperature range $3<T<300$ K and $3<T<170$ K for CMW and CMN respectively. The variable temperature NPD data do not show structural changes down to 3 K. Fig. 9 shows the thermal evolution of the unit-cell volume and ⟨Mn/B–O⟩ distances for both sites (2c and 2d). For both phases the volume steadily decreases with temperature. Very interestingly, the evolution of the average size of both octahedral positions is very distinct for both compounds. CMW shows no abrupt changes in both $\langle Mn_{2d}–O\rangle$ and $\langle(Mn/W)_{2c}–O\rangle$ distances. However for CMN, a distinct evolution is observed at lower temperatures. At RT these distances are slightly different and intermediate between the end $\langle Mn^{4+}/Nb^{5+}–O\rangle=1.92$ Å and $\langle Mn^{3+}/Nb^{5+}–O\rangle=2.02$ Å values at low temperature. This difference increases progressively at lower temperature down to 85 K, where the distances at sites 2c and 2d attain those expected for $\langle Mn^{4+}/Nb^{5+}–O\rangle$ and $\langle Mn^{3+}/Nb^{5+}–O\rangle$ respectively.

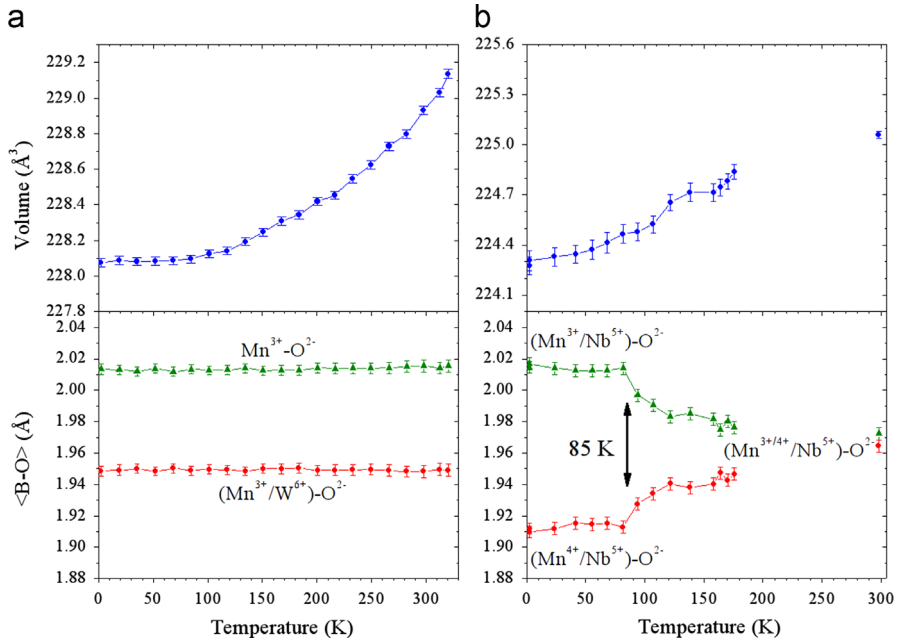

Fig. 9. Top panel, unit-cell volume as a function of temperature. Bottom panel, octahedral size ⟨B–O⟩ as a function of temperature for (a) $Ca_3Mn_2WO_9$ and (b) $Ca_3Mn_2NbO_9$.

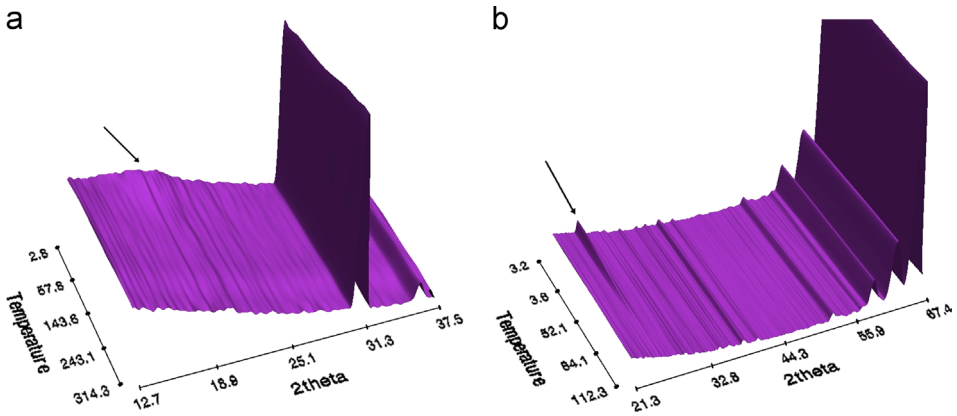

Fig. 10. Thermal evolution of NPD patterns, with λ=2.492 Å, collected sequentially for (a) $Ca_3Mn_2WO_9$ and (b) $Ca_3Mn_2NbO_9$. The arrows indicate the changes at low temperature for each sample.

This behaviour can be directly related to the anomalies observed in the transport and magnetic measurements. That observed at 160 K in the transport measurements can be associated with a charge order effect, which triggers an orbital rearrangement of the Mn^{3+} ions (Jahn–Teller effect) and also drives the anomaly detected in the magnetic measurements at 120 K. Finally, at 85 K the orbital ordering is stabilized, as observed in the ⟨Mn/Nb–O⟩ distances obtained from the NPD.

3.5.2. *Magnetic structure*

At low temperature both compounds present subtle changes in their NPD patterns due to weak magnetic contributions to the scattering. Fig. 10 shows the thermal evolution of the NPD patterns in the low 2θ-angle region. CMW does not present new peaks but some changes in the background intensity are observed, probably due to magnetic interactions that do not lead to long range magnetic ordering. Fig. 11(a) shows the Rietveld plot after refinement of the crystal structure of CMW at 3 K, where an arrow indicates the background change.

On the other hand, in CMN new peaks of magnetic origin appear below $\approx$40 K, which can be indexed with a propagation vector k=(0,0,0). The most intense peak is indicated with an arrow in Fig. 11(b). In order to obtain a magnetic model for this phase, we used the "*BasIreps*" programme (included in a *FullProf Suite* package) which calculates the possible magnetic couplings between Mn_{2c} and Mn_{2d} ions.

Thus, four possible couplings were obtained, which were tested to find the best fit of the magnetic peaks. Mn_{2d} presents two magnetic moments $Mn_{2d}{}^1$ and $Mn_{2d}{}^2$ at (1/2,0,0) and (0,1/2,1/2) positions respectively whose components are coupled, in the best fit, as: $m_x{}^1=-m_x{}^2$, $m_y{}^1=m_y{}^2$ and $m_z{}^1=-m_z{}^2$. The same coupling is present for $Mn_{2c}{}^1$ and $Mn_{2c}{}^2$ moments at (1/2,0,1/2) and (0,1/2,0) positions, respectively. We have constrained the scale factors of both structural and magnetic models, and refined the magnitude of the ordered Mn magnetic moments at both crystallographic positions. Fig. 11(b) shows the refinement of CMN at 3 K; a scheme of the magnetic structure is shown in the inset. The magnetic moments refined at 3 K are 2.0 and 1.2μ_B for 2*d* and 2*c* sites respectively. These values represent the magnetic moment per Mn atom in the ordered state and should be associated with the spin-only contribution.

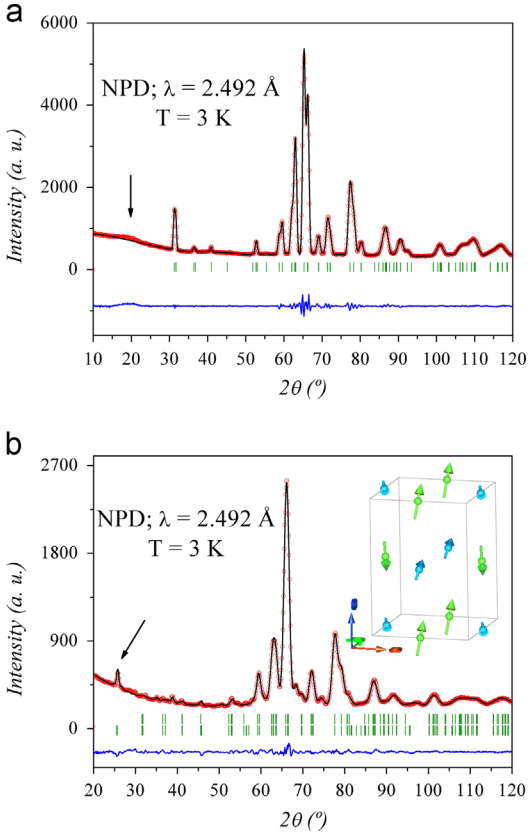

Fig. 11. Rietveld plots after the refinement of (a) the crystal structure of $Ca_3Mn_2WO_9$ and (b) the crystal and magnetic structure for $Ca_3Mn_2NbO_9$ from NPD data at T=3 K. The line at the bottom is the difference between calculated and experimental patterns. The upper set of bars corresponds to the Bragg reflections for the crystallographic phase and the lower (in (b)) correspond to the magnetic phase. The inset in (b) is a view of the magnetic structure of CMN obtained from the refinements. The arrows in (a) indicate the background intensity change and in (b) the main reflection of the magnetic structure.

4. Discussion

The crystal structures defined in the space group $P2_1/n$ of $Ca_3Mn_2WO_9$ and $Ca_3Mn_2NbO_9$, can ideally be rewritten as $Ca_2Mn_{1.33}W_{0.66}O_6$ and $Ca_2Mn_{1.33}Nb_{0.66}O_6$ respectively. These monoclinically distorted structures contain three non-equivalent oxygen atoms, the positions of which cannot be very accurately determined by XRPD as strong pseudo-symmetry is present in the patterns. A NPD study has been essential to investigate the subtle structural features of these perovskites, neutrons being more sensitive to the oxygen positions. This was particularly important in CMN due to the high disorder observed in the *B* site, where it was necessary to analyse in detail the nuclear density (by DFM) in order to assign the appropriate space group.

The refined site occupancies for both samples (Tables 1 and 2) show that the Mn/B'' long-range ordering is complete in CMW and negligible in CMN. Hence the degree of long-range ordering is DO=1 and 0.04 for CMW and CMN, respectively. Therefore, the crystallographic formulas obtained are:

$Ca_2[Mn]_{2d}[Mn_{0.33}W_{0.67}]_{2c}O_6$ (for CMW)

$Ca_2[Mn_{0.65}Nb_{0.35}]_{2d}[Mn_{0.68}Nb_{0.32}]_{2c}O_6$ (for CMN)

This can be simply explained from the larger charge difference between Mn^{3+} and W^{6+} present in CMW with respect to Mn^{3+}/Mn^{4+} and Nb^{5+} in CMN.

In CMN a charge-ordering effect between Mn^{3+} and Mn^{4+} octahedra has been detected by the structural evolution and physical properties. The sizes of the two types of octahedra in CMN become very different at low temperatures. For the 2*d* site, the average distance increases up to 2.02 Å (expected distance for Mn^{3+}–O, 2.045 Å)[27]. In parallel, the ⟨Mn/Nb–O⟩ bond-lengths for the 2*c* site decrease down to 1.91 Å, as expected for Mn^{4+}–O (expected distance for Mn^{4+}–O, 1.93 Å) [27]. This behaviour in the distances reveals a charge ordering effect (Mn^{3+}–Mn^{4+}) at low temperatures. The sequential refinement reveals a gradual change in the octahedral size, reaching a completely ordered state approximately at 85 K. This gradual ordering could be due to the inhomogeneities in the Mn–Nb distributions. The charge order allows us to better understand the magnetic behaviour observed in CMN, manifested as a change in the θ_{Weiss} value above and below of the charge ordering, whereas the Curie constant is not affected. The charge order also explains the subtle increase in the resistivity around to 160 K. In a charge ordered state the electrons become localized, leading to formation of a more insulating state. This change is clearly observed in Fig. 8, $(d\mathrm{Ln}(\rho)/d(kT)^{-1}$ vs. T plot).

In CMN, the intrinsic Mn/Nb disorder observed in this double perovskite generates regions rich in Mn cations, separated by diamagnetic Nb^{5+} cations. The magnetic interactions in these regions where $(Mn^{3+})_{2d}$–O–$(Mn^{4+})_{2c}$ couples are present could be understood as a system similar to the magnetic CE-type cell described by Goodenough for manganites [28]. This magnetic cell is similar to that observed in our case (see Fig. 11(b)). But the comparison is not complete, because the diamagnetic Nb^{5+} ions distributed at random in the structure restrict the magnetic order to isolated regions. This fact is supported by the reduced magnetic moments refined for the magnetic structure. The spin only contribution Mn^{3+} (HS) and Mn^{4+} are 4 and 3μ_B/Mn respectively, hence the magnetic moments per site expected would 2.6 and 2μ_B/site. However, the refined magnetic moments are 2.0 and 1.2μ_B/site for 2*d* and 2*c* respectively. This difference indicates that a fraction of Mn atoms are not magnetically ordered, due to the occurrence of isolated magnetic patches.

In CMW the superior Mn/W long-range ordering produces a much poorer magnetic ordering, limited to regions where Mn^{3+}–O–Mn^{3+} couples are present; this is observed by the absence of magnetic reflection in the low-temperature NPD pattern.

In both samples the magnetic behaviour is complex due to the competence between different magnetic coupling as: Mn–O–Mn and Mn–O–B''–O–Mn for B''=W or Nb, generating a certain degree of frustration. The difference between ZFC and FC magnetization curves measured at H=5 kOe (Fig. 7(a) and (b)), is a strong indication of the important magnetic frustrations at low temperature in both systems.

As seen above, the paramagnetic moments obtained from the Curie–Weiss fit are in accord with those expected for both samples. The Weiss temperatures obtained are +1.4 K and −99 K, giving clues about the sign of the magnetic interactions present in the solids. For CMW, lacking a long-range magnetic ordering although the magnetization suggests weak ferrimagnetic behaviour below 30 K, the θ_{Weiss} value is positive and close to 0. By contrast, for CMN, a non-collinear antiferromagnetic structure (with a ferrimagnetic component along the *b*-axis) is determined at low temperatures from NPD data, concomitant with a negative Weiss temperature.

Finally, the resistivity in both materials changes when an external magnetic field is applied. In our case the resistivity measurement as a function of magnetic field shows a non-negligible positive magnetoresistive effect at room temperature, reaching a maximum value of 0.5% and 1.2% for CMW and CMN respectively, with a magnetic field of 9 T. At lower temperatures the MR increases up to 11.5% for CMN at 100 K. This is in contrast with the negative MR described for $CaMn_{1-x}(Nb,W)_xO_3$ below the magnetic order temperature [29]; this effect has been extensively studied in manganites and it is associated with the spin scattering with the FM domains aligned to the external magnetic field. Also, this effect is completely different from the common positive MR observed in the majority of metals due to the cyclotron orbits, which presents very low values.

However, positive MR has been also observed in different polycrystalline oxides, as spinels ($MnTi_{2-x}V_xO_4$, $Mn_{2-x}V_{1+x}O_4$) [30,31], pyroclore ($Gd_2(Mo_{0.6}V_{0.4})_2O_7$) [32] and perovskites ($CaVO_3$) [33]. Also in films of VO_x and metallic doped ZnO or TiO_2 [34–36]. Practically in all the cases mentioned, the systems present some type of magnetic order. In $Ca_3Mn_2WO_9$ and $Ca_3Mn_2NbO_9$, we observed the phenomenon in the paramagnetic phase at high temperature far from the magnetic order transition. A similar behaviour, only has been found from $CaVO_3$ and $Mn_{2-x}V_{1+x}O_4$ [31,33]. This last presents a similar electrical property and their behaviour has been explained in terms of hopping of polarons [31]. This mechanism can be used in order to explain the transport properties in our samples. More studies are required to unveil the origin of the positive MR in the present systems.

5. Conclusions

The synthesis and crystal structure of two new manganese-based double perovskite oxides $Ca_3Mn_2B''O_9$ with B''=W and Nb have been reported by first time from XRPD and NPD. The initial refinements by XRPD indicate a maximum cationic order between Mn and W and a high degree of disorder between Mn and Nb, confirmed by NPD. For CMN the analysis of difference-Fourier allowed selecting the correct structural model in the $P2_1/n$ space group. The same symmetry is obtained for $Ca_3Mn_2WO_9$. The main difference in these samples is the oxidation states of manganese cations. CMW contain Mn^{3+} while CMN includes a mixed-valence between Mn^{3+} and Mn^{4+}. The amount of each oxidation state was confirmed by thermogravimetric analysis.

From the sequential neutron diffraction data in CMW the expected contraction of the cell parameters is observed, without change of the octahedral size. Contrarily, in CMN an interesting change in the octahedral size suggested a charge-ordering effect between Mn^{3+} and Mn^{4+}, segregated at low temperatures into two different crystallographic sites (2*d* and 2*c*). The magnetic and transport measurements support the charge-ordering behaviour observed from NPD for this intrinsically disordered double perovskite. The long-range magnetic order is weak in both samples and it occurs below 30 and 40 K for CMW and CMN, respectively. This magnetic order for both samples is hindered by the random distribution of diamagnetic ions (W^{6+} or Nb^{5+}). For this reason, only for CMN a weak magnetic contribution to the scattering is observed at low-temperatures, whereas in CMW no magnetic diffraction was observed. Moreover, one of the interesting properties in both samples is a positive magnetoresistance at room

temperature; for CMN a MR value as high as 11.5% at 100 K is observed under 9 T.

Acknowledgements

C.A.L. and M.E.S. thanks a CONICET fellowship. J.C.P. thanks CONICET (Project PIP 2008-01360), SECyT-UNSL (Project 7707 and Project 2-1612). R.D.S. acknowledges financial support of ANPCYT (Project PICT 2011-0752) and SEPCyT-UNCu (06/C389). J.C.P. and R.D.S are member of CONICET. J.A.A. acknowledges the financial support of the Spanish Ministry of Education to the project MAT2010-16404. We are grateful to I.L.L. for making all facilities available.

References

[1] C.N.R. Rao, B. Raveau, Transition Metal Oxides: Structure, Properties, and Synthesis of Ceramic Oxides, John Wiley & Sons, New York, 1998.
[2] B. Raveau, Prog. Solid State Chem. 35 (2007) 171–173.
[3] C.N.R. Rao, B. Raveau, Colossal Magnetoresistance, Charge Ordering and Related Properties of Manganese Oxides, World Scientific, Singapore, 1998.
[4] A.P. Ramirez, J.Phys.: Condes. Matter 9 (1997) 8171–8175.
[5] K.I. Kobayashi, T. Kimura, H. Sawada, K. Terakura, Y. Tokura, Nature 395 (1998) 677–680.
[6] D. Niebieskikwiat, R.D. Sánchez, A. Caneiro, L. Morales, M. Vásquez-Mansilla, F. Rivadulla, L. Hueso, Phys. Rev. B 62 (2000) 3340–3345.
[7] D. Niebieskikwiat, A. Caneiro, R.D. Sánchez, J. Fontcuberta, Phys. Rev. B 64 (2001) 1804061–1804064.
[8] M.C. Viola, J.A. Alonso, J.C. Pedregosa, R.E. Carbonio, Eur. J. Inorg. Chem. (2005) 1559–1564.
[9] M. Retuerto, J.A. Alonso, M.J. Martínez-Lope, M. García-Hernández, C.A. López, M.C. Viola, J.C. Pedregosa, M.T. Fernández-Díaz, Eur. J. Inorg. Chem. (2009) 3750–3757.
[10] R.M. Pinacca, M.C. Viola, J.C. Pedregosa, R.E. Carbonio, J.A. Alonso, J. Mater. Chem. 15 (2005) 4648–4653.
[11] M.S. Augsburger, M.C. Viola, J.C. Pedregosa, R.E. Carbonio, J.A. Alonso, J. Mater. Chem. 16 (2006) 4235–4242.
[12] C.A. López, M.C. Viola, J.C. Pedregosa, J.A. Alonso, M.T. Fernández-Díaz, Eur. J. Inorg. Chem. (2010) 4110–4120.
[13] M. Shikano, O. Ishiyama, Y. Inaguma, T. Nakamura, M. Itoh, J. Solid State Chem. 120 (1995) 238–243.
[14] D. Ballutaud-Harari, P. Poix, J. Solid State Chem. 14 (1975) 354–358.
[15] S.A. Larrégola, J.A. Alonso, R.M. Pinacca, M.C. Viola, J.C. Pedregosa, J. Solid State Chem. 181 (2008) 2808–2813.
[16] V.C. Fuertes, M.C. Blanco, D.G. Franco, J.M. De Paoli, R.D. Sánchez, R.E. Carbonio, Mater. Res. Bull. 46 (2011) 62–69.
[17] D.G. Franco, V.C. Fuertes, M.C. Blanco, M.T. Fernández-Díaz, R.D. Sánchez, R.E. Carbonio, J. Solid State Chem. 184 (2012) 385–391.
[18] H.M. Rietveld, J. Appl. Crystallogr. 2 (1969) 65–71.
[19] J. Rodríguez Carvajal, Physica B 192 (1993) 55–69.
[20] R.M. Hazen, L.W. Finger, J.W.E. Mariathasan, J. Phys. Chem. Solid 46 (1985) 253–263.
[21] I. Levin, J.Y. Chan, R.G. Geyert, J.E. Maslar, T.A. Vanderah, J. Solid State Chem. 156 (2001) 122–134.
[22] I.D. Brown, D. Altermatt, Acta Crystallogr. B 41 (1985) 244–247.
[23] J. Gonzales-Platas, J.Rodriguez-Carvajal, GFourier Program, Included in a Full-Prof Suite Package.
[24] I.Gil de Muro, M. Insausti, L. Lezama, T. Rojo, J. Solid State Chem. 178 (2005) 928–936.
[25] J.P. Cummings, S.H. Simonsen, Am. Mineralog. 55 (1970) 90–97.
[26] P.M. Woodward, Acta Crystallogr. B 53 (1997) 32–43.
[27] R.D. Shannon, Acta Crystallogr. A 32 (1976) 751–767.
[28] J.B. Goodenough, Phys. Rev. 100 (1955) 564–573.
[29] B. Raveau, Y.M. Zhao, C. Martin, M. Hervieu, A. Maignan, J. Solid State Chem. 149 (2000) 203–207.
[30] T. Sonehara, K. Kato, K. Osaka, M. Takata, T. Katsufuji., Phys. Rev. B 74 (2006) 1044241–1044247.
[31] E.V. Pannunzio-Miner, J.M De Paoli, R.E. Carbonio, R.D. Sánchez, J. Appl. Phys. 105 (2009) 1139061–1139068.
[32] I.O. Troyanchuk, N.V. Kasper, D.D. Khalyavin, H. Szymczak, A. Navialek, Phys. Status Solidi A 167 (1998) 151–155.
[33] H. Falcón, J.A. Alonso, M.T. Casais, M.J. Martinez-Lope, J. Sánchez-Benítez, J. Solid State Chem. 177 (2004) 3099–3104.
[34] A.D. Rata, V. Kataev, D. Khomskii, T. Hibma, Phys. Rev. B 68 (2003) 2204031–2204034.
[35] A.G. Petukhov, M. Foygel, Phys. Rev. B 62 (2000) 520–531.
[36] Y. Matsumoto, M. Murakami, T. Shono, T. Hasegawa, T. Fukumura, M. Kawasaki, P. Ahmet, T. Chikyow, S. Koshihara, H. Koinuma, Science 291 (2001) 854–856.